Res Chem Intermed (2016) 42:6449–6481
DOI 10.1007/s11164-016-2474-2

Synthesis, characterization, antimicrobial activity and ultrastructure of the affected bacteria of new quinoline compounds

A. Z. El-Sonbati[2] · M. I. Abou-Dobara[1] · M. A. Diab[2] · A. A. El-Bindary[2] · S. G. Nozha[2]

Received: 21 October 2015 / Accepted: 1 February 2016 / Published online: 29 February 2016

Abstract The reaction on 8-hydroxy quinoline-7-aldehyde azo compounds (HL_n) (where $n = 1$–5) with 4-amino-1,2-dihydro-2,3-dimethyl-1-phenylpyrazol-5-one to obtain HL_n (where $n = 6$–10) have been characterized by means of TLC, melting point and spectral data, such as IR, ^{1}H NMR, mass spectra and thermal studies. The X-ray diffraction patterns of two starting materials 8-hydroxy quinoline-7-aldehyde (start 1), 4-amino-1,2-dihydro-2,3-dimethyl-1-phenylpyrazol-5-one (start 2) and the ligands ($HL_{5,10}$) are investigated in powder form. All the ligands have been screened for their antimicrobial activity against four local bacterial species, two Gram-positive bacteria (*Bacillus cereus* and *Staphylococcus aureus*) and two Gram-negative bacteria (*Escherichia coli* and *Klebsiella pneumoniae*) as well as against four local fungi; *Aspergillus niger*, *Alternaria alternata*, *Penicillium italicum* and *Fusarium oxysporium*. The results show that the azo ligands (HL_n) (where $n = 1$–5) have no antimicrobial activity against bacteria and fungi while most azomethine ligands (HL_n) (where $n = 6$–10) are good antibacterial agents against *E. coli* and *K. pneumoniae* as well as antifungal agents against *P. italicum* and *A. alternata*. The results were compared to standard substances (start 1) and (start 2). Among the azomethine ligands, HL_{10} was the most effective against the most microorganisms tested. The size of clear zone was ordered as p-($OCH_3 < CH_3 < H < Cl < NO_2$) as expected from Hammett's constant (σ^R). Also, the ultrastructure study of the affected bacteria confirmed that HL_8 is good antibacterial agent against *E. coli* and *S. aureus*.

S. G. Nozha: Abstracted from her Ph.D. Thesis.

✉ A. Z. El-Sonbati
elsonbatisch@yahoo.com

[1] Botany Department, Faculty of Science, Damietta University, Damietta, Egypt

[2] Chemistry Department, Faculty of Science, Damietta University, Damietta, Egypt

Keywords Azo Schiff bases · Azo quinoline · Azomethine · Antimicrobial activities · Ultrastructure

Introduction

Azo dyes constitute one of the largest and most varied groups of synthetic organic dyes in use today [1]. The major classes of dyes have anthroquinoid, indigoid and azo aromatic compounds. The chemical structure of azo dyes is comprised of a conjugated system of double bonds and aromatic rings. All these structures allow strong π–π* transitions in the UV–visible (UV–Vis) area, with high extinction coefficients. The drawback of these dyes is that they are not easily degraded by aerobic bacteria, and with the action of anaerobic or microaerobic reductive bacteria, they can form toxic or mutagenic compounds such as aromatic amines [2–4].

In addition, Schiff bases are some of the most widely used organic compounds. They are used as pigments and dyes, catalysts, intermediates in organic synthesis and as polymer stabilizers [5]. Schiff bases have also been shown to exhibit a broad range of biological activities, including antifungal, antibacterial, antimalarial, antiproliferative, anti-inflammatory, antiviral and antipyretic properties [5–8]. It has been suggested that azomethine linkage (C=N) might be responsible for the biological activities of Schiff bases [9].

Because of excellent yield and fast reaction, many researchers have developed azo Schiff base compounds and studied their properties and different applications [10, 11].

The quinoline nucleus has gathered immense attention among chemists as well as biologists as it is one of the key building elements for many naturally occurring compounds [12], while 8-hydroxyquinolines have been explored as a viable drug discovery platform in many instances. They can exert their physiological properties through bidentate chelation of metal ions [13].

Different quinoline compounds have been tested against fungi, a range of Gram-positive and Gram-negative bacteria, including *Staphylococcus aureus* and *Escherichia coli* [14–16]. Lam et al. [14] synthesized and characterized various derivatives of 8-hydroxyquinoline and studied their potential antibacterial activity against Gram-positive *S. aureus* and Gram-negative *E. coli*. They found that these quinoline compounds had no effect on *E. coli*, while showing antibacterial effect against *S. aureus*. They found that the synthetic 5,7-dibromo-2-methylquinolin-8-ol derivative shows a similar minimum inhibitory concentration (MIC) of 6.25 μg/mL as compared to that of methicillin (3.125 μg/mL) against *Staphylococcus aureus*. El-Behery et al. [15] synthesized a Schiff base hydrazone derived from 7-chloro-4-hydrazinoquinoline and its complexes with Cu(II), Ni(II), Co(II), Fe(III), and UO_2(II) ions. Also, they tested the Schiff base ligand and its metal complexes against one stain Gram-positive bacteria (*S. aureus*), Gram-negative bacteria (*E. coli*), and yeast (*Candida albicans*) and they found that, their compounds exhibited higher antibacterial acivities. Abou-Dobara et al. [16] studied the antimicrobial activity of azodye ligands) and their complexes [Cu(II)/Ni(II)] against four local bacterial and fungal species. They reported that these azodye compounds

have good antibacterial activity against *B. cereus, E. coli* and *K. pneumonia*e, the complexes were being more toxic than ligands against fungi and Cu^{2+} complexes were being more active than Ni^{2+} complexes against *B. cereus*, *E. coli* and *K. pneumoniae*.

In view of the facts mentioned above, a new series of azo Schiff bases of 8-hydroxyquinoline-7-aldehyde azodye ligands with 4-amino-1,2-dihydro-2,3-dimethyl-1-phenylpyrazol-5-one were synthesized and have been evaluated for their antimicrobial activity. Azodye ligands of 8-hydroxyquinoline-7-aldehyde and its derivatives have been prepared and characterized by elemental analyses, ^{1}H-NMR and IR spectra [17].

The aim of the present work is to synthesize 4-{[5-(4-substituted-phenylazo)-8-hydroxy-quinolin-7-ylmethylene]-amino}-1,5-dimethyl-2-phenyl-1,2-dihydropyrazol-3-one derivatives (HL_n) (where $n = 6$–10), and then test the antimicrobial activity of the $HL_{(1–10)}$ ligands against two Gram-positive and two Gram-negative bacteria in addition to four different types of fungi. The effect of HL_8 on the ultrastructure of two affected bacteria is also investigated.

Experimental

Materials

4-Amino-1,2-dihydro-2,3-dimethyl-1-phenylpyrazol-5-one and various aniline or *p*-substituted anilines were purchased from Aldrich, and the other chemicals were of analytical grade quality.

Preparation of (5-(4′-derivatives phenyldiazo)-8-hydroxy-7-quinolinecarboxaldehyde) ($HL_{1–5}$)

8-Hydroxy-7-quinolinecarboxaldehyde was prepared according to El-Sonbati and El-Bindary [18]. (5-(4′-derivatives phenylazo)-8-hydroxy-7-quinolinecarboxaldehyde) HL_n where ($n = 1$–5) prepared according to El-Sonbati et al. [17, 19] (Table 1). Azo dye ligands (HL_n) were prepared from aniline or its *p*-substituted derivatives (10 mmol) dissolved in hydrochloric acid (20 mmol/25 ml distilled

Table 1 Physical properties and elemental analysis data of quinoline azodyes ligands HL_n ($n = 1$–5)

Compound[a]	Yield %	Color	Exp. (calc) %		
			C	H	N
HL_1	55.22	Dirty brown	66.6 (66.5)	4.2 (4.2)	13.5 (13.7)
HL_2	58.38	Reddish brown	70.0 (70.1)	4.6 (4.5)	14.6 (14.4)
HL_3	69.4	Dark brown	69.4 (69.3)	3.9 (4.0)	15.0 (15.2)
HL_4	76.12	Light brown	61.5 (61.6)	3.2 (3.2)	13.3 (13.5)
HL_5	90.67	Dark red	59.7 (59.6)	3.0 (3.1)	17.5 (17.4)

[a] The analytical data agree satisfactorily with the expected formulae as given in Fig. 1

H_2O). The hydrochloric compound was diazotized below 0–5 °C with a solution of sodium nitrite (0.8 g, 10 mmol, 30 ml distilled H_2O). The diazonium chloride was coupled with an alkaline solution of oxine (1.7 g, 10 mmol) in 20 ml of pyridine. The crude dye was collected by filtration and was crystallized from DMF, then dried in a vacuum desiccator over P_2O_5. The preparation of (HL_{1-5}) is summarized in Fig. 1.

Preparation of 4-{[5-(4-methoxy-phenylazo)-8-hydroxy-quinolin-7-ylmethylene]-amino}-1,5-dimethyl-2-phenyl-1,2-dihydro-pyrazol-3-one (HL_{6-10})

Ethanolic solutions of 4-amino-1,2-dihydro-2,3-dimethyl-1-phenylpyrazol-5-one (0.1 mol) and [5-(4′-derivatives phenyldiazo)-8-hydroxy-7-quinolinecarboxaldehyde)] (HL_1–HL_5) (0.1 mol) were refluxed for 4 h over a steam bath. The excess solvent was removed by evaporation and the concentrated solution was cooled in an ice bath with stirring. The azo Schiff base (HL_n) separated out as a colored powder and was recrystallized from ethanol, then dried in a vacuum desiccator over P_2O_5. The purity of the ligands was checked by TLC. Our synthetic route of azo Schiff base ligands is shown in Scheme 1. The color, yield % and analytical data are given in Table 2.

The resulting formed ligands are:

(5-(4′-methoxyphenylazo)-8-hydroxy-7-quinolinecarboxaldehyde) (HL_1)
(5-(4′-methyl phenylazo)-8-hydroxy-7-quinolinecarboxaldehyde) (HL_2)
(5-(4′-phenylazo)-8-hydroxy-7-quinolinecarboxaldehyde) (HL_3)
(5-(4′-chlorophenylazo)-8-hydroxy-7-quinolinecarboxaldehyde) (HL_4)
(5-(4′-nitrophenylazo)-8-hydroxy-7-quinolinecarboxaldehyde) (HL_5)
4-{[5-(4-methoxy-phenylazo)-8-hydroxy-quinolin-7-ylmethylene]-amino}-1,5-dimethyl-2-phenyl-1,2-dihydro-pyrazol-3-one (HL_6)

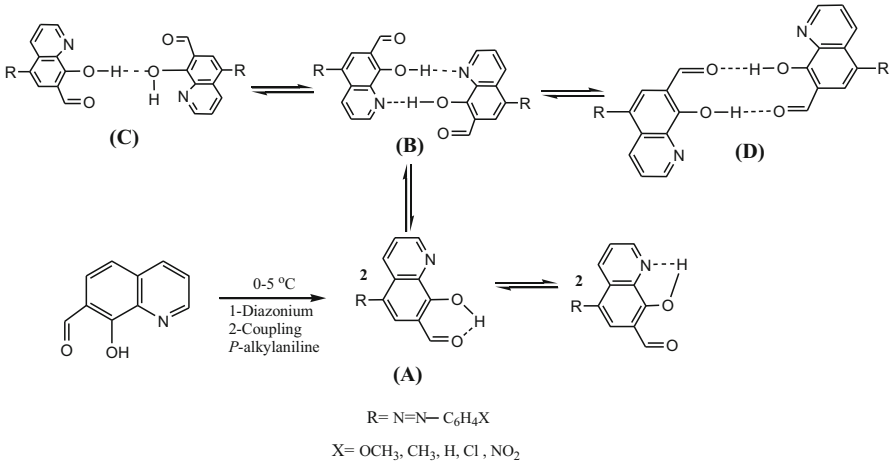

Fig. 1 Structure for the dimmer and tautomer forms of 8-hydroxy-7-quinoline-carboxaldehyde azodyes (HL_{1-5})

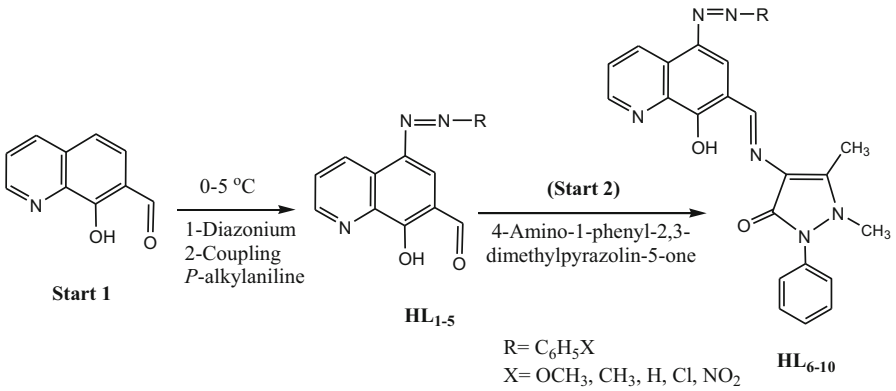

Scheme 1 Synthetic route of azo Schiff base ligands HL_n (where $n = 6$–10)

Table 2 Physical properties and elemental analysis data of quinoline azo Schiff base ligands HL_n ($n = 6$–10)

Compound[a]	Yield %	Color	Exp. (calc) %		
			C	H	N
HL_6	39	Pale yellow	68.13 (68.29)	4.64 (4.88)	16.82 (17.07)
HL_7	40.7	Dark yellow	70.47 (70.59)	4.90 (5.04)	17.37 (17.65)
HL_8	43.3	Bright yellow	70.01 (70.13)	4.54 (4.76)	17.79 (18.18)
HL_9	46.6	Dark orange	65.14 (65.26)	4.12 (4.23)	16.68 (16.92)
HL_{10}	53	Dark brown	63.84 (63.91)	4.03 (4.14)	19.08 (19.33)

[a] The analytical data agree satisfactory with the expected formulae represented as given in Scheme 1

4-{[5-(4-methyl-phenylazo)-8-hydroxy-quinolin-7-ylmethylene]-amino}-1,5-dimethyl-2-phenyl-1,2-dihydro-pyrazol-3-one (HL_7)
4-{[5-(4-phenylazo)-8-hydroxy-quinolin-7-ylmethylene]-amino}-1,5-dimethyl-2-phenyl-1,2-dihydro-pyrazol-3-one (HL_8)
4-{[5-(4-chlorophenylazo)-8-hydroxy-quinolin-7-ylmethylene]-amino}-1,5-dimethyl-2-phenyl-1,2-dihydro-pyrazol-3-one (HL_9)
4-{[5-(4-nitrophenylazo)-8-hydroxy-quinolin-7-ylmethylene]-amino}-1,5-dimethyl-2-phenyl-1,2-dihydro-pyrazol-3-one (HL_{10}).

Microbiological investigation

For this investigation, the agar well diffusion method was applied [20]. The antibacterial activities of the investigated compounds were tested against two local Gram-positive bacteria (*B. cereus* and *S. aureus*) and two local Gram-negative bacteria (*E. coli* and *K. pneumoniae*) on nutrient agar medium. Also, the antifungal effect was tested against four local fungal species (*Aspergillus niger*, *Alternaria alternata*, *Penicillium italicum* and *Fusarium oxysporium*) on DOX agar medium. The concentrations of each solution were 50, 100 and 150 µg/mL. By using a sterile

cork borer (10 mm diameter), wells were made in agar medium plates previously seeded with the test microorganism. Then, 200 µl of each compound was applied in each well. The agar plates were kept at 4 °C for at least 30 min to allow the diffusion of the compound, then incubated at 30 °C or 37 °C for bacteria and fungi, respectively. Penicillin and miconazole were used as antibacterial and antifungal substrates, respectively. The diameters of inhibition zones were determined after 24 h for bacteria and after 7 days for fungi. For electron microscopic study, overnight cultures of *E. coli* and *S. aureus* were subjected to 150 µg/mL of HL_8 for 2 h. Non-treated (control) bacteria and DMF-treated bacteria were also included. After that, bacterial cells were centrifuged and washed with distilled water. The bacteria were fixed with formalin-glutaraldehyde fixative ($_4F_1G$) in 0.1 M phosphate buffer pH 7.4. After rinsing in the buffer, samples were post-fixed in 2 % OsO_4 for 2 h at 4 °C in the same buffer. The cells were washed and dehydrated at 4 °C through a graded series of ethanol. Cells were then treated with propylene oxide solution and embedded in a mixture of 1:1 of Epon-Araldite for 1 h. Polymerization was done in the oven at 65 °C for 24 h. Ultrathin sections (50 µm) were cut on an ultratome (Model LKB), then mounted on copper grids, double-stained with uranyl acetate and lead citrate and investigated on a JEOL 100CX (TEM).

Measurements

Elemental microanalyses of the separated ligands chelates for C, H and N were performed in the Microanalytical Center at Cairo University, Egypt. The analyses were repeated twice to check the accuracy of the analyzed data. Melting or decomposition points were carried out on a melting point apparatus. The ^{1}H-NMR spectrum was obtained with a JEOL FX90 Fourier transform spectrometer with DMSO-d_6 as the solvent and TMS as an internal reference. Infrared spectra were recorded as KBr pellets using a Pye Unicam SP 2000 spectrophotometer. Ultraviolet–visible (UV–Vis) spectra of the compounds were recorded in Nujol mulls using a Unicom SP 8800 spectrophotometer. X-ray diffraction patterns of the powder forms were recorded on X-ray diffractometer (Philips x'pert) with Ni-filtered CuKα-radiation ($\lambda = 1.5418$ Å) in the range of diffraction angle ($2\theta^\circ = 4^\circ$–70°). The applied voltage and the tube current are 30 kV and 30 mA, respectively. Mass spectra were recorded by the EI technique at 70 eV using MS-5988 GS-MS Hewlett-Packard. Thermal studies were computed on Simultaneous Thermal Analyzer (STA) 6000 system using thermogravimetric analysis (TGA) method. Thermal properties of the samples were analyzed in the temperature range from 30 to 800 °C at the heating rate of 10 °C/min under dynamic nitrogen atmosphere.

Morphometric analysis

Morphometric analyses were achieved by using UTHSCSA Image tool software for Wndows v.3.

Statistical analysis

All the data of morphometric analysis are expressed as mean ± SE. The statistical significance was evaluated by ANOVA using SPSS v.10 and the individual comparisons were obtained by the LSD method at 0.05 significance levels.

Results and discussion

Characterization of azo dye ligands HL_n (n = 1–5)

The structure of [5-(4′-derivatives phenylazo)-8-hydroxy-7-quinolinecarboxaldehyde] HL_n where (n = 1–5) using various physico-chemical properties like color, yield and elemental analysis which are given in Table 1. The elemental analytical data of ligands agreed well with the calculated values as shown in Fig. 1.

The ^{1}H NMR spectra of quinolone and its alkyl derivatives found two signals in the ~9.10–12.43 and ~8.89–9.28 ppm regions assigned to δ(OH) and δ(CN), respectively. ^{1}H NMR studies for the free ligands under investigation in DMSO-d_6 also show two signals at δ 9.3–9.7 and 8.95–9.3 ppm which are similar to those observed previously [21–24]. Those signals are also assigned to the protons of OH and CN, respectively, in the spectra of the free ligands under investigation. The –OH proton signals exhibit fast exchange in the presence of D_2O, i.e., it disappeared in the presence of D_2O and this is attributed to the strongly hydrogen bonding as in Fig. 1. The shifts are in the sequence: p-NO_2 > p-Cl > H > p-CH_3 > p-OCH_3. In the ^{13}C NMR spectra, there is no detectable signal for the carbon of carbonyl group (C=O) at the quinoline ring for the hydrazone form. Also, two broad bands (OH signals) were determined from the azo form of ligands in the ^{1}H NMR spectrum. The signal for the N–H proton of ligands for the hydrazone form was not observed in DMSO-d_6. The singlet peaks at 56.32 ppm are due to the methoxy (OCH_3)

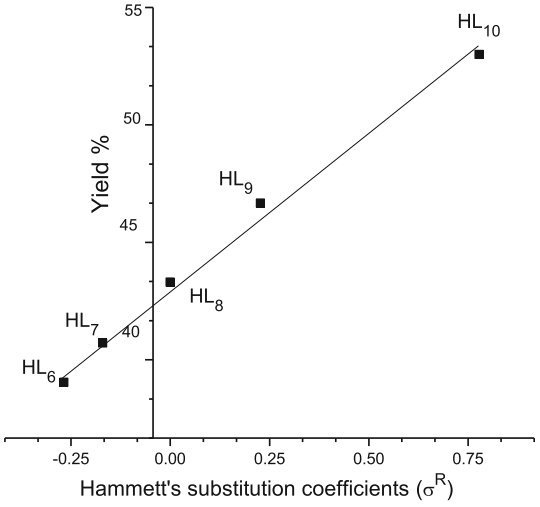

Fig. 2 The relationship between Hammett's substitution coefficients (σ^R) versus yield % of azo Schiff base ligands (HL_n, n = 6–10)

carbons. The aromatic carbons (C=C), hydroxyl rings and aldehydic group are observed in the extensive 111.5–153.2 ppm range.

The electronic spectra of HL_n ligands exhibited bands at 32,500–32,150 cm^{-1} (CN) (π–π*), 33,450–33,340 cm^{-1} (H-bonding and association), 40,038–39,460 cm^{-1} (phenyl) (Ph–Ph*, π–π*) [20] and 29,340–29,230 cm^{-1} transition of phenyl rings overlapped by composite broad (π–π*) of the azo structure. The band due to the $n \rightarrow \pi^*$ transition obtained in the visible region is associated mainly with the color of the respective compound [23]. The analytical data and the spectral properties of the ligands are consistent with their structure in Fig. 1.

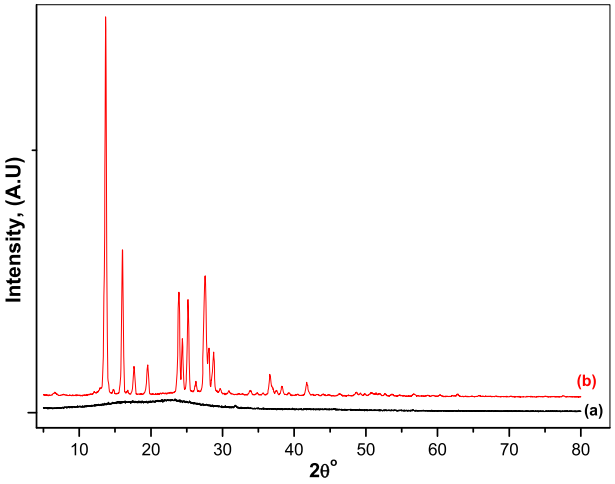

Fig. 3 X-ray diffraction pattern for two starts: **a** start 1 and **b** start 2

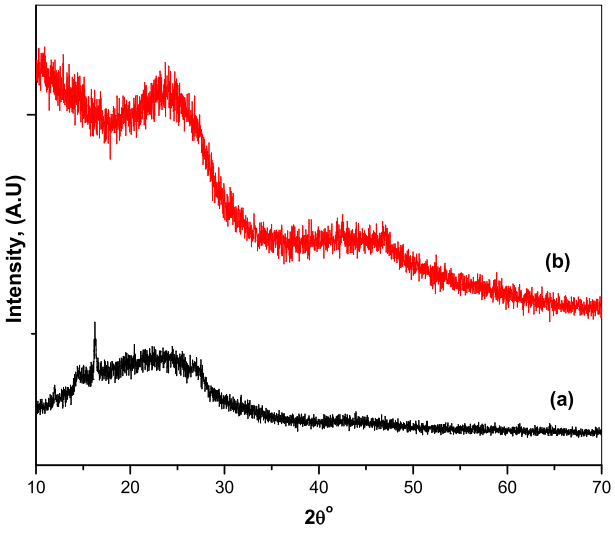

Fig. 4 X-ray diffraction pattern for (HL_5 and HL_{10}) ligand derivatives: **a** HL_5 and **b** HL_{10}

Characterization of azo Schiff base ligands HL_n (n = 6–10)

The ligands ($HL_{6–10}$) were prepared by stirring an appropriate amount of reactive *p*-derivatives 8-hydroxy quinoline-7-aldehyde (azo compounds) with the corresponding 4-amino-1,2-dihydro-2,3-dimethyl-1-phenylpyrazol-5-one in ethanol. The formed Schiff base azo ligands ($HL_{6–10}$) were characterized with respect to their composition by elemental and spectral analysis. All five ligands $HL_{6–10}$, gave

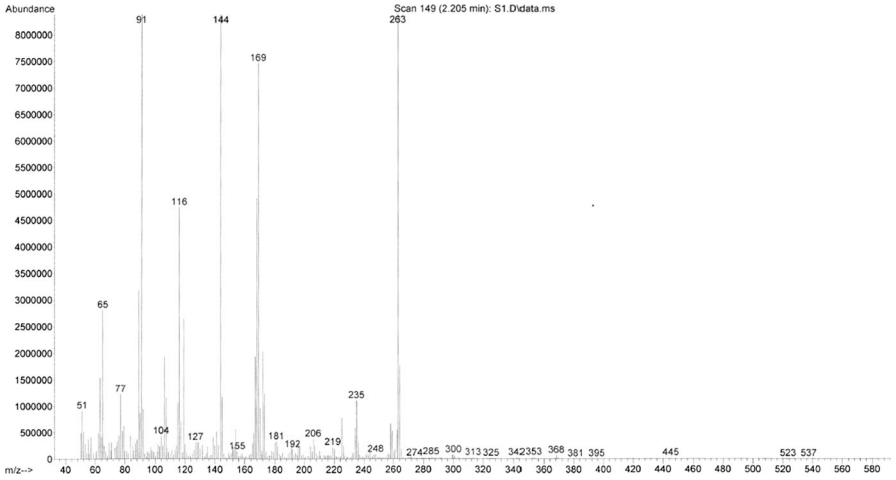

Fig. 5 Mass spectrum of HL_2 ligand

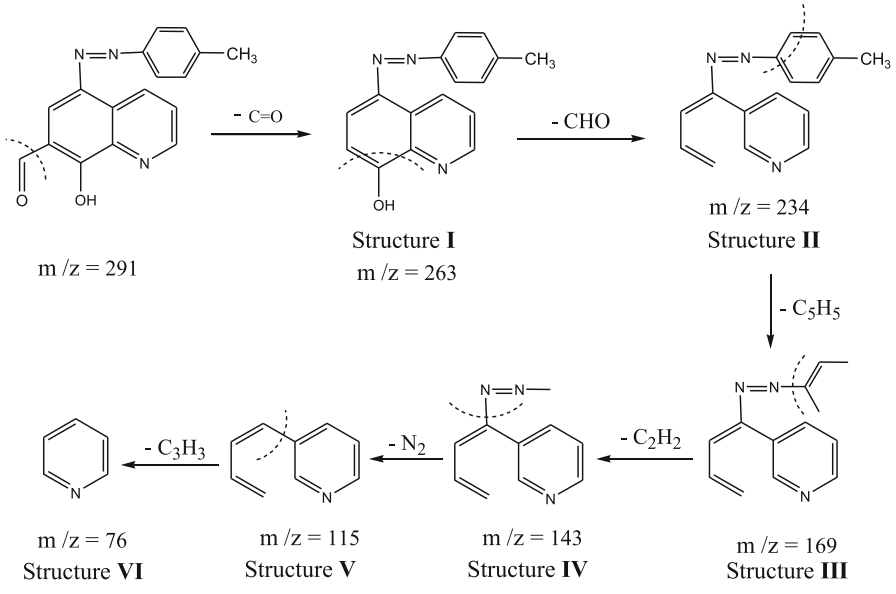

Scheme 2 Fragmentation patterns of HL_2 ligand

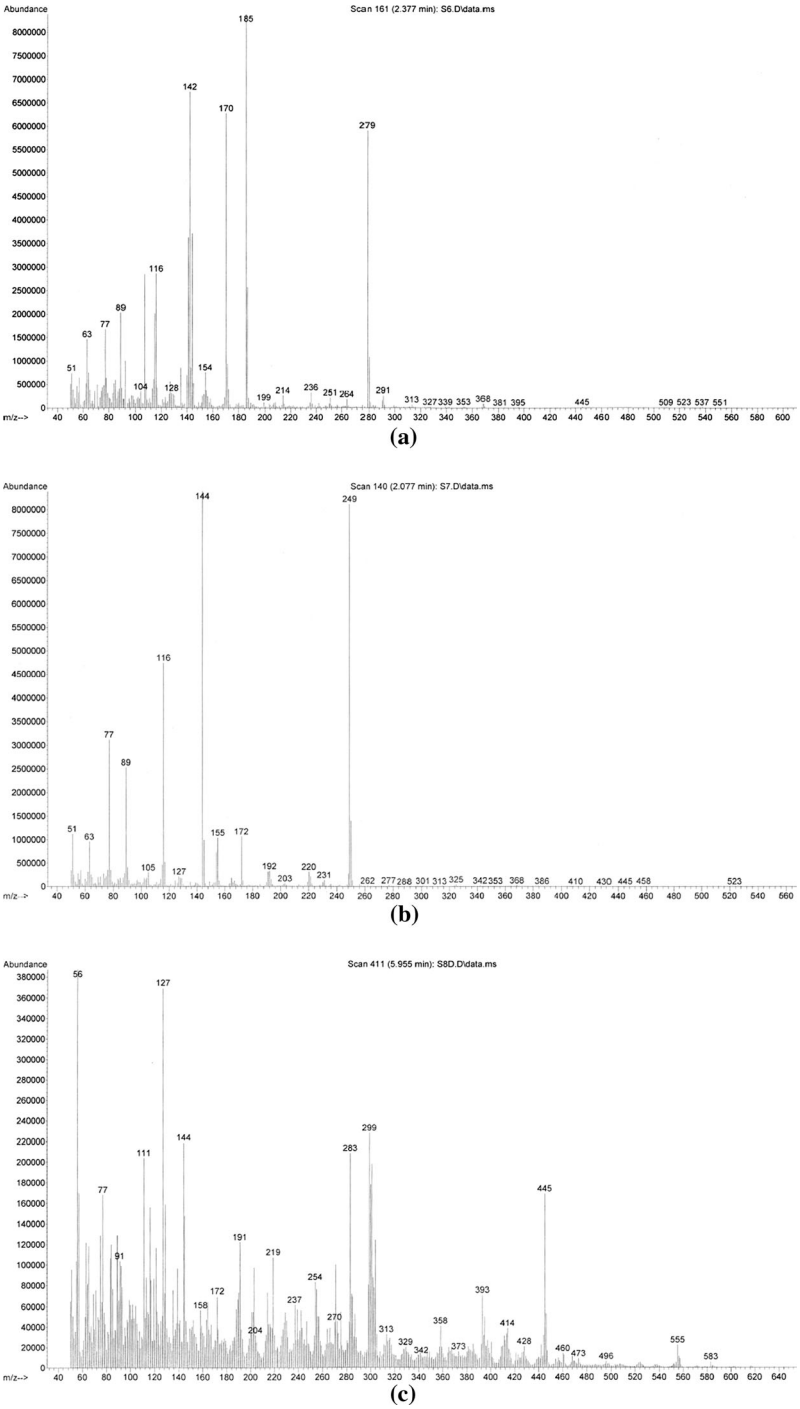

Fig. 6 Mass spectrum of **a** HL_6 ligand, **b** HL_8 ligand, **c** HL_9 ligand

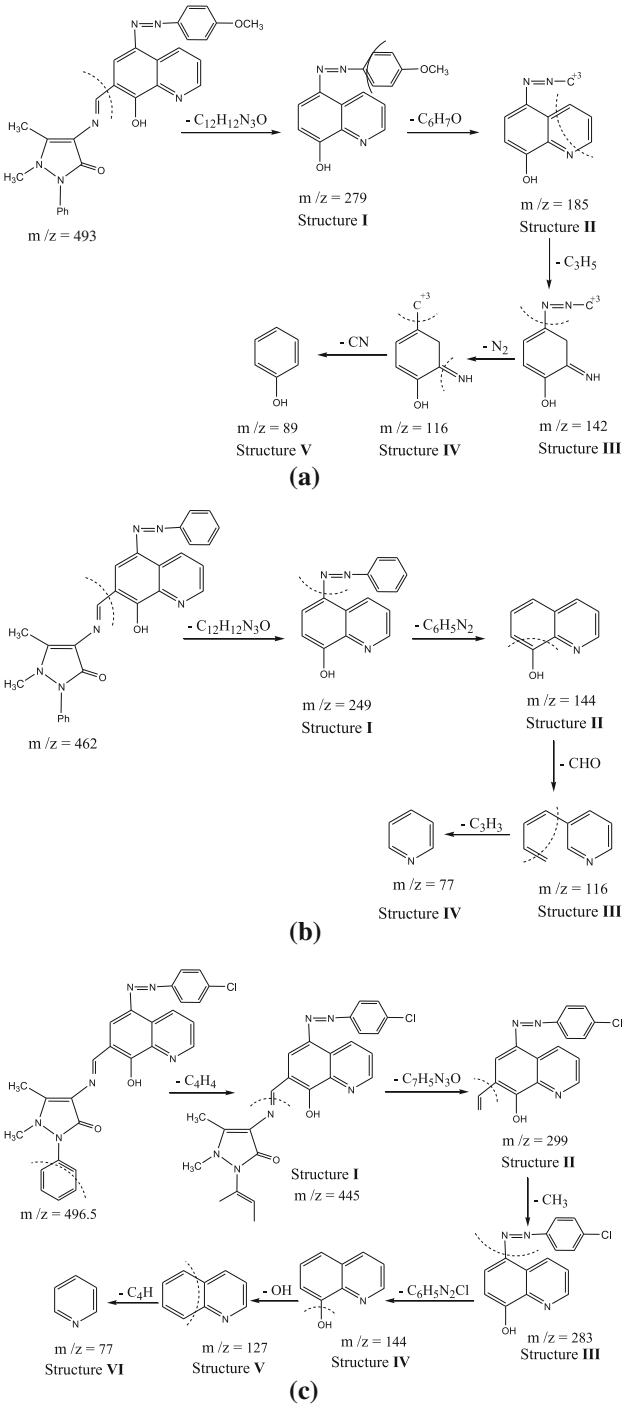

Scheme 3 Fragmentation patterns of **a** HL_6 ligand, **b** HL_8 ligand, **c** HL_9 ligand

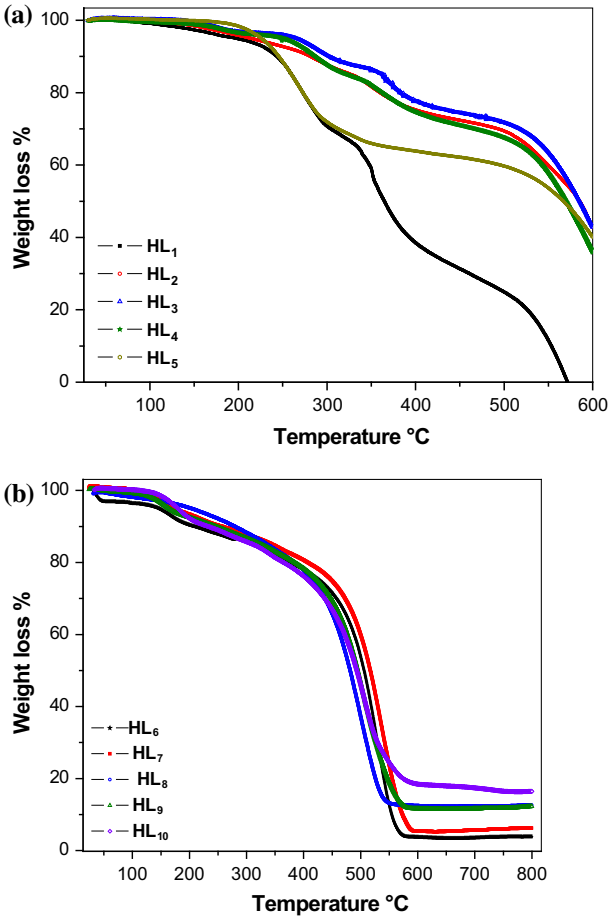

Fig. 7 Thermogravimetric analysis (TGA) for ligands. **a** $HL_{1–5}$ and **b** $HL_{6–10}$

satisfactory elemental analyses (Table 2). Detailed solution and solid state studies of these ligands were carried out to establish their geometry.

As shown in Table 2, the values of yield % is related to the nature of the *p*-substituent as they increase according to the following order *p*-(NO_2 > Cl > H > CH_3 > OCH_3). This can be attributed to the fact that the effective charge experienced by the d-electrons increased due to the electron-withdrawing *p*-substituent (HL_9 and HL_{10}) while it decreased with the electron-donating character of (HL_6 and HL_7). This is in accordance with that expected from Hammett's substitution coefficients (σ^R), as in Fig. 2 the yield % values correlate with (σ^R), and it is clear that all these values increase with increasing σ^R [22–26].

Table 3 Thermal decomposition data for azo quinoline ligands (HL_{1-5})

Compound	Temp. range (°C)	Found mass loss (calc) (%)	Assignment
HL_1	35–291	27.35 (24.72)	Evaluation of CO + loss of OH & OCH_3
	291–389	31.95 (33.80)	Decomposition of $C_6H_4N_2$
	389–620	40.99 (41.0)	Decomposition of C_9H_4N
	>620	–	Ash
HL_2	120–400	24 (23.36)	Decomposition of C_4H_6N
	400–620	40.89 (39.52)	Decomposition of $C_4H_7N_2O_2$
	>620	34.33 (32.98)	Loss of 8C
HL_3	134–305	10.64 (10.09)	Evaluation of CO
	305–618	56.8 (56.62)	Loss of OH + decomposition of $C_9H_4N_2$
		OH (6.13)	
		$C_9H_4N_2$ (50.49)	
	>620	32.56 (32.45)	Decomposition of C_6H_4N
HL_4	55–202	3.6 (4.17)	Decomposition of CH
	202–423	23.8 (22.8)	Decomposition of $C_3H_3O_2$
	423–620	48 (49.9)	Decomposition of $C_6H_6N_3Cl$
	>620	24.64 (23.12)	Loss of 6C
HL_5	170–299	28.43 (28.22)	Evaluation of CO + Loss of OH & NO_2
		CO (8.68)	
		OH (5.27)	
		NO_2 (14.27)	
	299–620	39.30 (39.09)	Decomposition of C_9H_4N
	>620	32.27 (32.27)	Decomposition of $C_6H_4N_2$

X-ray diffraction analysis

The X-ray diffraction patterns (XRD) of 8-hydroxy quinoline-7-aldehyde (start 1), 4-amino-1,2-dihydro-2,3-dimethyl-1-phenylpyrazol-5-one (start 2) and the ligands (HL_5 and HL_{10}) in powder form are shown in Figs. 3 and 4, respectively. Broad peaks for start 1 at $2\theta = 16°$ and 23° indicating an amorphous structure (Fig. 3a). Many peaks are observed which indicate the polycrystalline nature of start 2 (Fig. 3b). According to Fig. 4, the XRD patterns of (HL_5 and HL_{10}) show that the peak appeared at $2\theta = 16°$ for HL_5 is a mixture of amorphous and polycrystalline structures (Fig. 4a), while HL_{10} is completely amorphous with two peaks appearing at $2\theta = 24°$ and 45° (Fig. 4b).

Mass spectra

The electron impact mass spectrum of HL_2, HL_6, HL_8 and HL_9 ligands were recorded and investigated at 70 eV of electron energy. For HL_2, It is obvious that the molecular ion peaks are in good agreement with their suggested empirical formulae as indicated from the elemental analysis (Table 1). The mass spectrum

Table 4 Thermal decomposition data for azo Schiff base quinoline ligands (HL_{6-10})

Compound	Temp. range (°C)	Found mass loss (calc) (%)	Assignment
HL_6	35–46	2 (2.64)	Loss of CH
	46–570	92.357 (92.48)	Decomposition of $C_{25}H_{23}N_6O_3$
	570–800	4.685 (4.878)	Loss of 2C
HL_7	100–240	9.22 (8.82)	Decomposition of C_3H_6
	240–590	85.12 (85.29)	Decomposition of $C_{23}H_{14}N_6O_2$
	590–800	6.28 (5.88)	Decomposition of C_2H_4
HL_8	50–170	2.97 (2.81)	Loss of CH
	170–550	83.26 (83.11)	Decomposition of $C_{21}H_{16}N_6O_2$
	550–800	13.2 (14.06)	Decomposition of C_5H_5
HL_9	105–170	4.82 (5.24)	Decomposition of C_2H_2
	170–580	82.3 (81.66)	Decomposition of $C_{20}H_{14}N_6O_2Cl$
	580–800	12.3 (13.09)	Decomposition of C_5H_5
HL_{10}	120–200	7.5 (7.69)	Decomposition of C_3H_3
	200–580	72.79 (72.97)	Decomposition of $C_{17}H_4N_7O_4$
	580–800	19.47 (19.33)	Decomposition of C_7H_{14}

Table 5 The values of the E_d, of HL_n (where $n = 1$–10) according to the Arrhenius relationship

Compound	E_d (kJ mol^{-1})
HL_1	22.91583
HL_2	40.12523
HL_3	142.1689
HL_4	29.44023
HL_5	143.2887
HL_6	50.80982
HL_7	51.81592
HL_8	18.60734
HL_9	44.23005
HL_{10}	40.58675

fragmentation mode of ligand (HL_2) shows the exact mass of 291 corresponding to the formula $C_{17}H_{13}N_3O_2$ (Fig. 5). The ion of $m/z = 291$ undergoes fragmentation to a stable peak at $m/z = 263$ by losing C=O atoms (structure **I**) as shown in Scheme 2. The loss of CHO leads to the fragmentation with $m/z = 234$ (structure **II**). The loss of C_5H_5 atoms leads to the fragmentation with $m/z = 169$ (structure **III**). The loss of C_2H_2 atoms leads to the fragmentation with $m/z = 143$ (structure **IV**). A breakdown of the backbone of HL_2 ligand gives the fragments (**V**) and (**VI**).

It is obvious that the molecular ion peaks for ligands (HL_6, HL_8 and HL_9) are in good agreement with their suggested empirical formula as indicated from the

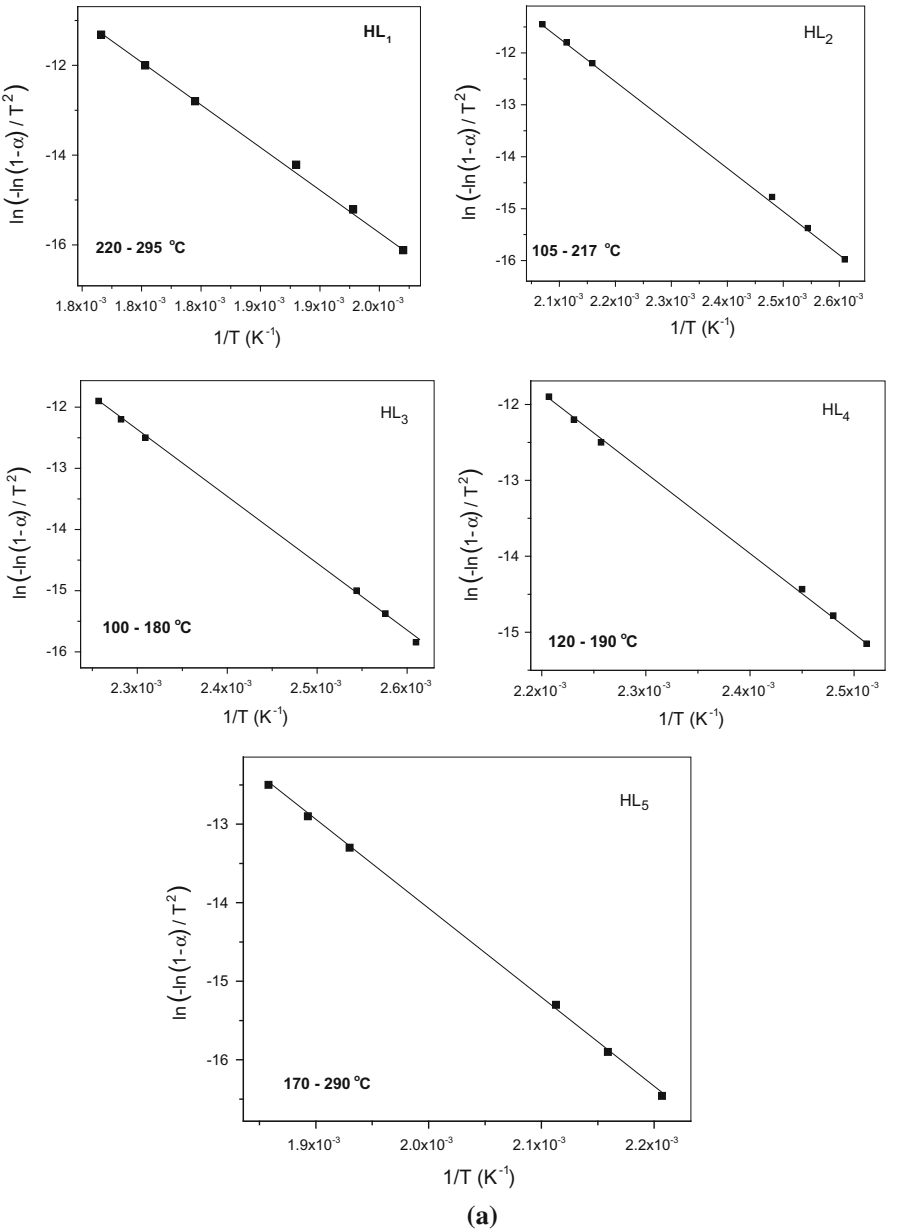

Fig. 8 Coats–Redfern (CR) of azo ligands **a** (HL_n, $n = 1$–5), **b** (HL_n, $n = 6$–10)

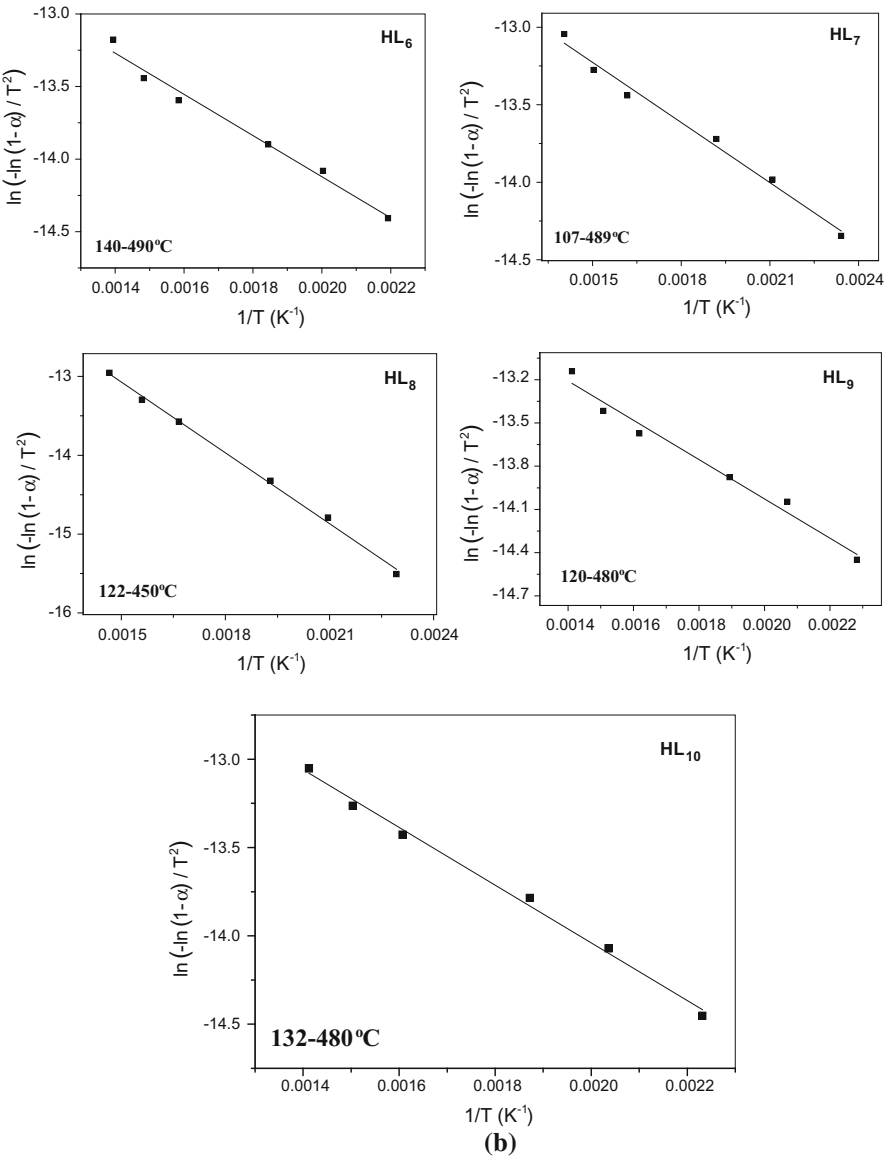

Fig. 8 continued

elemental analysis (Table 2). The mass spectrum fragmentation mode of ligand (HL_6) shows the exact mass of 493 corresponding to the formula $C_{28}H_{25}N_6O_3$ (Fig. 6a). The ion of $m/z = 493$ undergoes fragmentation to a stable peak at $m/z = 279$ by losing $C_{12}H_{12}N_3O$ atoms (structure **I**) as shown in Scheme 3a. The loss of C_6H_7O leads to the fragmentation with $m/z = 185$ (structure **II**). The loss of

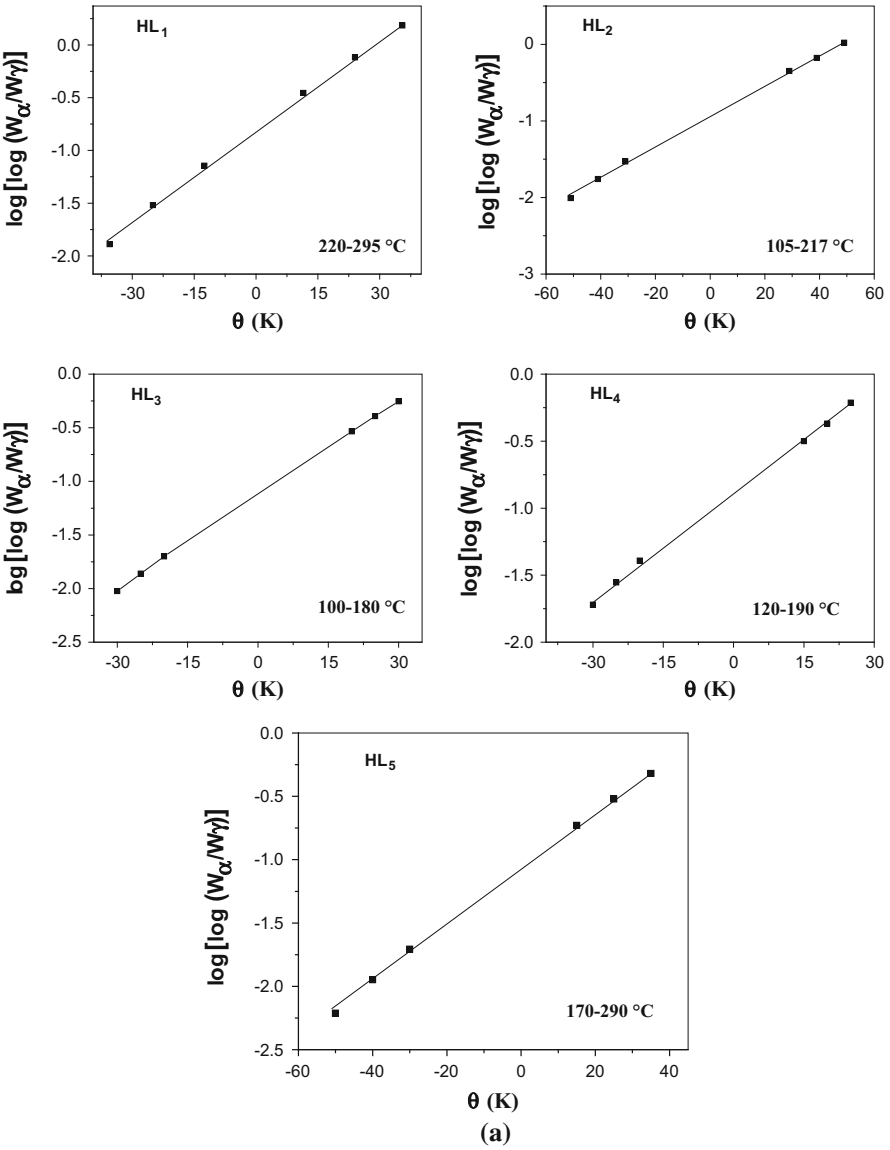

Fig. 9 **a** Horowitz–Metzger (HM) of azo ligands (HL_n, $n = 1$–5). **b** Horowitz–Metzger (HM) of azo Schiff base ligands (HL_n, $n = 6$–10)

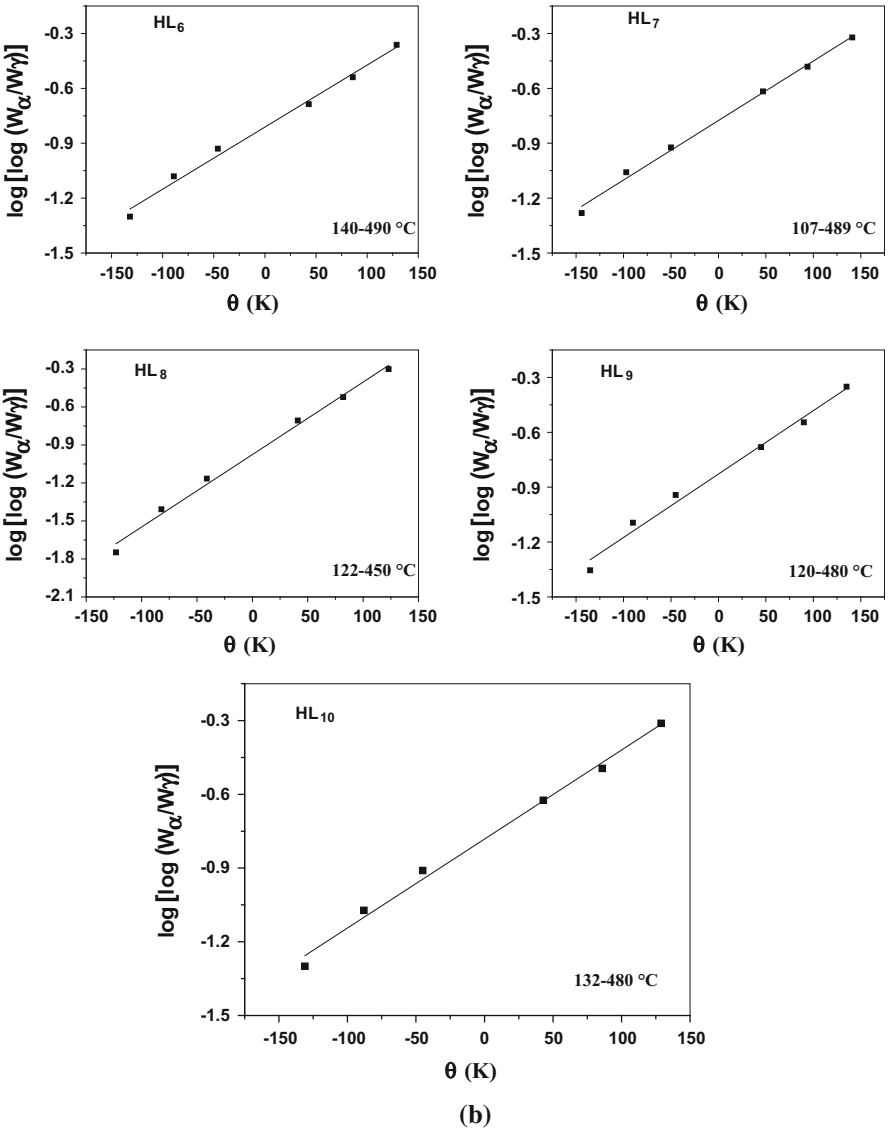

(b)

Fig. 9 continued

C_3H_5 atoms leads to the fragmentation with $m/z = 142$ (structure **III**). A breakdown of the backbone of HL_6 ligand gives the fragments (**IV**) and (**V**).

The mass spectrum fragmentation mode of ligand (HL_8) shows the exact mass of 462 corresponding to the formula $C_{27}H_{22}N_6O_2$ (Fig. 6b). The ion of $m/z = 462$ undergoes fragmentation to a stable peak at $m/z = 249$ by losing $C_{12}H_{12}N_3O$ atoms (structure **I**) as shown in Scheme 3b. The loss of $C_6H_5N_2$ leads to the fragmentation

with *m/z* = 144 (structure **II**). A breakdown of the backbone of HL_8 ligand gives the fragments (**III**) and (**IV**).

The mass spectrum fragmentation mode of ligand (HL_9) shows the exact mass of 496.5 corresponding to the formula $C_{27}H_{21}N_6O_2Cl$ (Fig. 6c). The ion of *m/z* = 496.5 undergoes fragmentation to a stable peak at *m/z* = 445 by losing C_4H_4 atoms (structure **I**) as shown in Scheme 3c. The loss of $C_7H_5N_3O$ leads to the fragmentation with m/z = 299 (structure **II**). The loss of CH_3 atoms leads to the fragmentation with *m/z* = 283 (structure **III**). The loss of $C_6H_5N_2Cl$ atoms leads to the fragmentation with *m/z* = 144 (structure **IV**). A breakdown of the backbone of HL_9 ligand gives the fragments (**V**) and (**VI**).

Thermogravimetric analysis

The TGA curves of azo ($HL_{1–5}$) and azo Schiff base ligands ($HL_{6–10}$) are shown in Fig. 7(a and b), respectively. It is clear from these figures that the change of azo group to azomethine strongly affects the decomposition behavior. The detailed analysis of the behavior of decomposition for both azo ($HL_{1–5}$) and azo Schiff base

Table 6 Thermodynamic activation energy for all ligands ($HL_{1–10}$)

Compound[a]	Temp. range (°C)	Method	Parameter				
			E_a (kJ mol^{-1})	A (s^{-1})	ΔS* (J mol^{-1} K^{-1})	ΔH* (kJ mol^{-1})	ΔG* (kJ mol^{-1})
HL_1	220–295	CR	155	1.06E+13	−3.38E−01	150	150
		HM	156	3.96E+13	1.06E+01	152	146
HL_2	105–217	CR	69	6.34E+05	−1.37E+02	65.4	125
		HM	72.3	5.69E+06	−1.19E+02	68.6	120
HL_3	100–180	CR	91	9.76E+08	−7.55E+01	87.6	119
		HM	96.1	2.38E+10	−4.90E+01	92.7	113
HL_4	120–190	CR	86.8	1.75E+08	−9.01E+01	83.3	122
		HM	93.7	4.13E+09	−6.38E+01	90.1	117
HL_5	170–290	CR	93.7	1.31E+07	−1.13E+02	89.5	146
		HM	107	1.66E+09	−7.27E+01	103	139
HL_6	140–490	CR	11.8	4.46E−03	−2.96E+02	6.9	181
		HM	22.5	1.93E−01	−2.64E+02	17.6	173
HL_7	107–489	CR	10.8	2.70E−03	−2.99E+02	6.01	177
		HM	20.3	8.97E−02	−2.70E+02	15.6	170
HL_8	122–450	CR	24.9	9.40E−02	−2.70E+02	20.3	171
		HM	34.3	3.52E+00	−2.40E+02	29.7	164
HL_9	120–480	CR	11.3	2.81E−03	−2.99E+02	6.57	178
		HM	21.8	1.30E−01	−2.67E+02	17.1	170
HL_{10}	132–480	CR	13.6	5.69E−03	−2.93E+02	8.76	179
		HM	23.2	1.74E−01	−2.65E+02	18.4	172

[a] The number corresponds to that used in Tables 1 and 2

($HL_{6–10}$) ligands are presented in Tables 3 and 4, respectively. For azo ligands $HL_{1–5}$, the TGA curves shown in Fig. 7a reveal that the decomposition process starts at a temperature in the range 150–200 °C depending on the function group, while in the first stage of heating, HL_1 (*p*-OCH_3) losses about 4.873 % of its weight, this loss can be attributed to the loss of moisture adsorbed in the matrix [22]. TGA curves of azo Schiff base ligands $HL_{6–10}$ shows three steps of decomposition as shown in Fig. 7b. The decomposition process starts at temperature in the range 35–240 °C depending on the function group.

More results about the degradation process can be extracted from the TGA curves as follow. The rate constant of the thermal degradation (K) is given by the Arrhenius relationship [22]:

Table 7 Antibacterial activity data of HL_n (where n = 6–10)

Compound	Conc. (μg/mL)	Gram-positive bacteria		Gram-negative bacteria	
		Bacillus cereus	*Staphylococcus aureus*	*Escherichia coli*	*Klebsiella pneumoniae*
Start 1	50	−ve	1	2	2
	100	−ve	−ve	2	2
	150	1	−ve	2	−ve
Start 2	50	−ve	1	2	1
	100	−ve	−ve	2	2
	150	−ve	−ve	2	−ve
HL_6	50	−ve	−ve	2	−ve
	100	−ve	−ve	3	−ve
	150	−ve	−ve	2	1
HL_7	50	−ve	−ve	2	−ve
	100	1	1	2	2
	150	−ve	1	3	1
HL_8	50	−ve	1	−ve	−ve
	100	−ve	1	3	−ve
	150	−ve	1	3	−ve
HL_9	50	−ve	−ve	2	−ve
	100	−ve	1	2	−ve
	150	−ve	−ve	2	2
HL_{10}	50	−ve	−ve	3	1
	100	−ve	−ve	3	1
	150	−ve	−ve	4	1
Penicillin	50	1	2	1	−ve
	100	3	2	3	−ve
	150	3	2	3	−ve

The results were recorded as the diameter of inhibition zone (mm)

$$\ln K = \ln A - E_d/RT$$

where R is a gas constant (=8.314 JK^{-1} mol^{-1}) and E_d the thermal activation energy of decomposition. The values of E_d for HL_{1-5} azo ligands and azo Schiff base ligands HL_{6-10} can be obtained by plotting ln K as a function of $1/T$. The values of E_d of HL_n (=−R.slope) are found to be in the range (22.92–143.28) for HL_{1-5} and in the range (18.6–51.8) for HL_{6-10}, respectively, as shown in Table 5. The high values of E_d for HL_{1-5} than HL_{6-10} indicate that the azo ligands are more stable than the Schiff base ligands.

Calculation of activation thermodynamic parameters

The thermodynamic activation parameters of decomposition processes of the azo (HL_{1-5}) and azo Schiff base ligands (HL_{6-10}), namely activation energy (E_a), enthalpy (ΔH^*), entropy (ΔS^*), and Gibbs free energy change of the decomposition (ΔG^*), are evaluated graphically by employing the Coast–Redfern [27] and Horowitz–Metzger [28] methods.

Coast–Redfern equation

The Coast–Redfern equation, which is a typical integral method, can be represented as:

$$\int_0^a \frac{dx}{(1-\alpha)^n} = \frac{A}{\phi}\int_{T_1}^{T_2} \exp\left(-\frac{E_a}{RT}\right) dt \quad (1)$$

For the convenience of integration, the lower limit T_1 is usually taken as zero. This equation on integration gives:

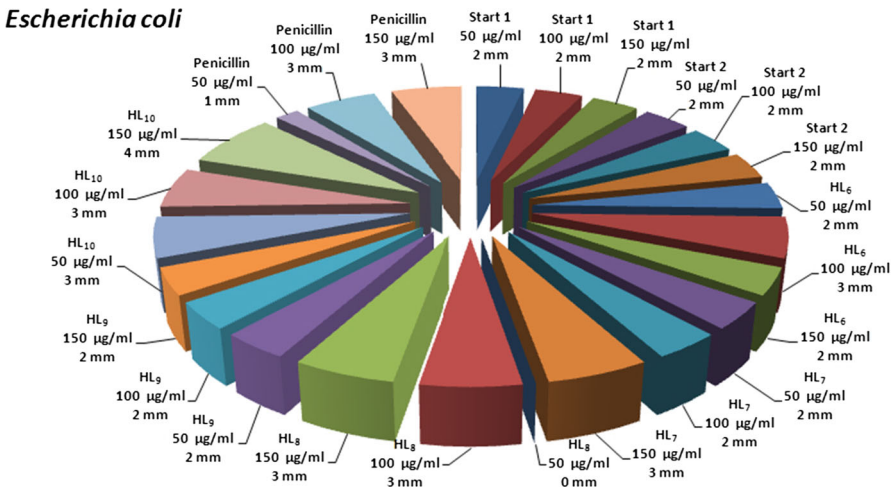

Fig. 10 Antibacterial activity data of azo Schiff base ligands (HL_n, $n = 6–10$) and its two starting materials, namely 8-hydroxy-7-formylquinoline (start 1) and 4-amino-1-phenyl-2,3-dimethylpyrazolin-5-one (start 2), against *Escherichia coli*. Inhibition zone was recorded as mm

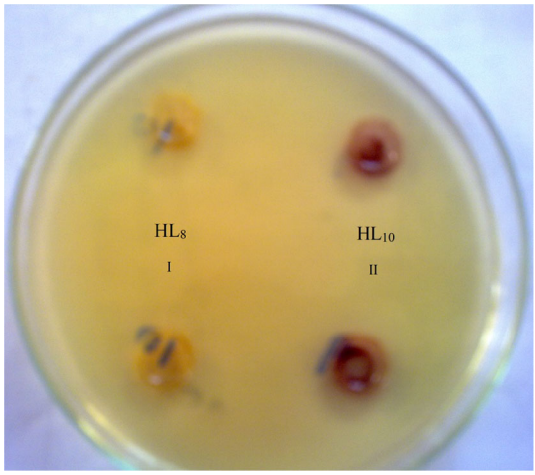

Fig. 11 Effect of HL_8 and HL_{10} on growth of *E. coli* on nutrient agar using concentration I = 100 μg/mL, II = 150 μg/mL

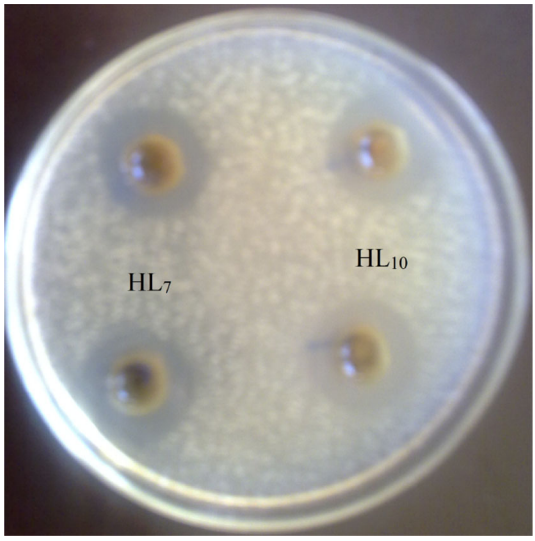

Fig. 12 Effect of HL_7 and HL_{10} on growth of *K. pneumoniae* on nutrient agar using concentration = 100 μg/mL

$$\ln\left[-\frac{\ln(1-\alpha)}{T^2}\right] = -\frac{E_a}{RT} + \ln\left[\frac{AR}{\phi E_a}\right] \tag{2}$$

A plot of the left-hand side (LHS) against $1/T$ was drawn for the azo ligands (HL_{1-5}) and azo Schiff base ligands (HL_{6-10}) in Fig. 8a and b, respectively. E_a is the energy of activation in J mol^{-1} and calculated from the slope and A in (s^{-1}) from the intercept value. The entropy of activation (ΔS^*) in (J mol^{-1} K^{-1}) was calculated by using the equation:

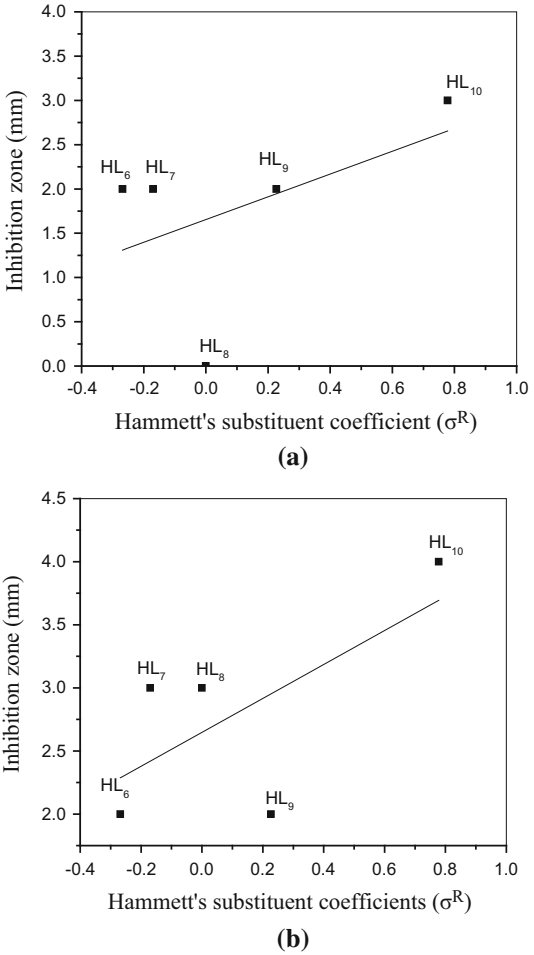

Fig. 13 The relationship between Hammett's substitution coefficients (σ^R) versus the inhibition zone (mm) of ligands (HL_n, $n = 6$–10) (in cases of *E. coli* at concentrations 50 μg/mL (**a**) and 150 μg/mL (**b**))

$$\Delta S^* = 2.303\left[\log\left(\frac{Ah}{k_B T_s}\right)\right]\mathrm{R} \tag{3}$$

where k_B is the Boltzmann constant, h is the Plank's constant and T_s is the TG peak temperature.

Horowitz–Metzger equation

The Horowitz–Metzger equation is illustrative of the approximation methods. These authors derived the relationship:

Table 8 Antifungal activity data of HL_n (where $n = 6$–10)

Compound	Conc. (μg/mL)	*Aspergillus niger*	*Fusarium oxysporum*	*Alternaria alternata*	*Penicillium italicum*
Start 1	50	−ve	1	7	2
	100	−ve	−ve	2	2
	150	−ve	−ve	2	1
Start 2	50	−ve	−ve	5	3
	100	−ve	2	−ve	2
	150	−ve	−ve	−ve	2
HL_6	50	−ve	−ve	−ve	4
	100	−ve	−ve	5	2
	150	−ve	−ve	−ve	−ve
HL_7	50	−ve	−ve	−ve	5
	100	−ve	1	−ve	1
	150	−ve	−ve	7	1
HL_8	50	−ve	−ve	−ve	5
	100	−ve	−ve	−ve	3
	150	−ve	3	−ve	−ve
HL_9	50	−ve	−ve	−ve	1
	100	−ve	3	−ve	−ve
	150	−ve	−ve	7	1
HL_{10}	50	−ve	−ve	−ve	3
	100	−ve	1	7	2
	150	−ve	−ve	7	1
Miconazole	50	1	2	5	1
	100	3	3	6	1
	150	4	3	6	2

The results were recorded as the diameter of inhibition zones (mm)

$$\log\left[\frac{1-(1-\alpha)^{1-n}}{1-n}\right] = \frac{E_a\theta}{2.303RT_s^2}, \quad \text{for } n \neq 1 \tag{4}$$

when $n = 1$, the LHS of Eq. (4) would be $\log[-\log(1-\alpha)]$ as shown in Fig. 9a and b, respectively, for ($HL_{1–5}$) and ($HL_{6–10}$). For a first-order kinetic process, the Horowitz–Metzger equation may be written in the form:

$$\log\left[\log\left(\frac{W_\alpha}{W\gamma}\right)\right] = \frac{E_a\theta}{2.303RT_s^2} - \log 2.303 \tag{5}$$

where $\theta = T - T_s$, $w_\gamma = w_\alpha - w$, w_α = mass loss at the completion reaction; w = mass loss up to time t. The plot of log [log (w_α/w_γ)] versus θ was drawn and

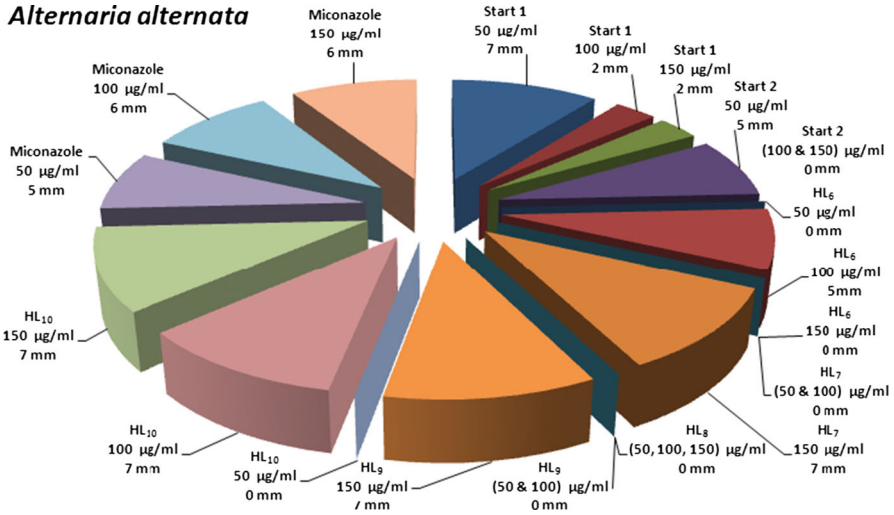

Fig. 14 Antifungal activity data of azo Schiff base ligands (HL_n, $n = 6$–10) and its two started materials, namely 8-hydroxy-7-formylquinoline (start 1) and 4-amino-1-phenyl-2,3-dimethylpyrazolin-5-one (start 2) against *Alternaria alternata*. Inhibition zone was recorded as mm

Table 9 Morphometric analysis of bacterial cells treated with HL_8

Treatment	*E. coli*			*S. aureus*	
	Cell length	Cell width	Distance between cell wall and cell membrane	Cell diameter	Cell wall thickness
Control	474.7 ± 30.7	243.3 ± 5.5	17.6 ± 1.9	334.9 ± 18.7	14.6 ± 1
DMF	465.8 ± 11.4	249.3 ± 2.8	19.5 ± 0.6	274.2 ± 16*	19 ± 1.1*
HL_8	433 ± 74.8	199.9 ± 13.1*	22.5 ± 2.4	300.8 ± 3.8	16.8 ± 0.6

* Significantly different at 0.05 level

found to be linear from the slope from which E_a was calculated. The pre-exponential factor, A, calculated from equation:

$$\frac{E_a}{RT_s^2} = \frac{A}{\left[\phi \exp\left(-\frac{E_a}{RT_s}\right)\right]} \tag{6}$$

The entropy of activation, ΔS^*, is calculated from Eq. (3). The enthalpy activation, ΔH^*, and Gibbs free energy, ΔG^*, are calculated from:

$$\Delta H^* = E_a - RT \tag{7}$$

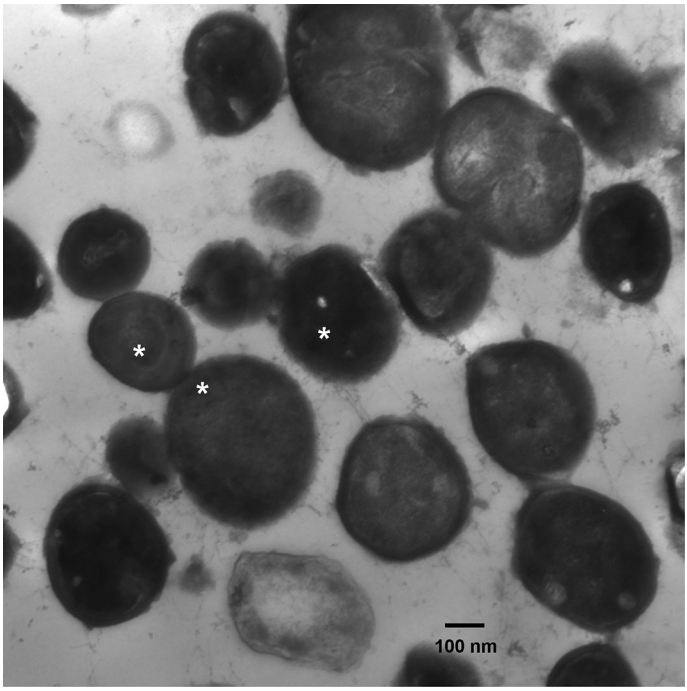

Fig. 15 Transmission electron micrograph of normal *S. aureus* illustrating different size of cocci cells, normal thin electron dense cell walls, homogenous electron dense cytoplasm, normal division and numerous ribosomes (*asterisks*). (Specimen fixed in $_4F_1G$ solution and double-stained with uranyl acetate and lead citrate; original magnification ×7500)

$$\Delta G^* = \Delta H^* - T\Delta S^* \tag{8}$$

The calculated values of E_a, A, ΔS^*, ΔH^* and ΔG^* for the decomposition steps for azo ligands (HL_{1-5}) and azo Schiff base ligands (HL_{6-10}) are summarized in Table 6. The entropy of activation energies reflects the thermal stability of the compounds. The entropy of activation is found to have negative values in the HL_n (where $n = 1–10$), which indicate that the decomposition reactions proceed spontaneously [29, 30]. The value of ΔG^* is positive, considered as a favorable or spontaneous reaction.

From the values of the energy of activation (E_a) of all the ligands (HL_{1-10}), it is observed that the azo ligands (HL_{1-5}) are more stable than the azo Schiff base ligands (HL_{6-10}).

Microbiological investigation

The Gram-negative rods have been implicated in infections as diverse as pneumonia to ear infections. One of the more common Gram-negative rods that cause disease in humans is *E. coli*. According to Bailey and Scott's "Diagnostic Microbiology," *E. coli*

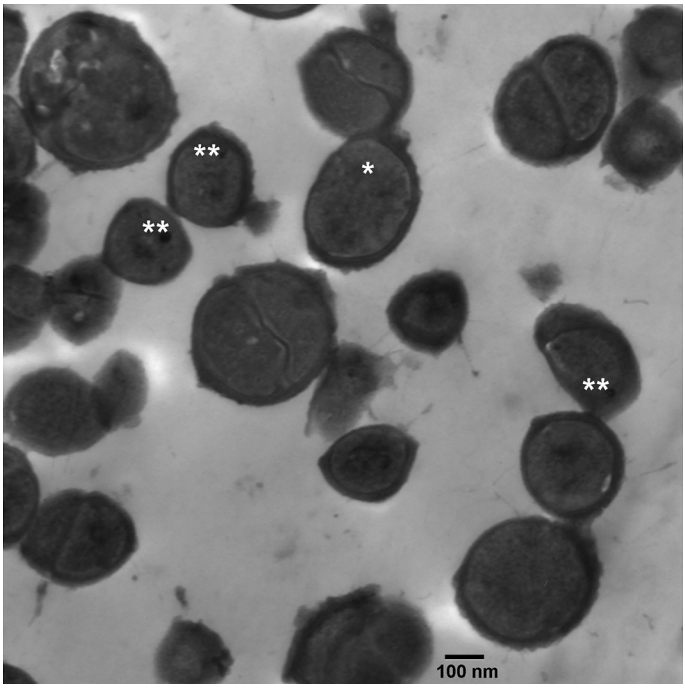

Fig. 16 Transmission electronic micrograph of *S. aureus* treated with DMF illustrating decreased size of cocci cells, electron dense boundary cell wall increased in thickness, numerous ribosomes (*single asterisks*), electron dense granules (*double asterisks*) and increased number of cells forming division septa. (Specimen fixed in $_4F_1G$ solution and double-stained with uranyl acetate and lead citrate; original magnification ×7500)

is by far the most common cause of uncomplicated community-acquired urinary tract infections and is frequently seen in wound infections. Certain strains of *E. coli* (such as *E. coli* O157:H7) can cause serious diarrhea and kidney damage [31, 32].

The antimicrobial activity of HL_n (where $n = 1–10$) ligands were tested against bacteria and fungi; we used more than one test organism to increase the chance of detecting their antimicrobial activities. The used organisms in the present investigations included two Gram-positive bacteria (*B. cereus* and *S. aureus*) and two Gram-negative bacteria (*E. coli* and *K. pneumoniae*) in addition to four species of fungi; (*A. niger*, *P. italicum, A. alternata* and *F. oxysporium*).

None of the used azo ligands (HL_n) (where $n = 1–5$) were found to have any antibacterial activity. However, the used azo Schiff base ligands (HL_n) (where $n = 6–10$) were found to have antibacterial activity. The results of the antibacterial activities of the synthesized azo Schiff base ligands ($HL_{6–10}$) are recorded in Table 7.

According to Table 7, $HL_{6–10}$ have antibacterial activity against *E. coli* (inhibition zone of $HL_6 = 2$ and 3 mm at concentrations = 50 and 100 μg/mL, respectively), (inhibition zone of $HL_7 = 2$ mm at concentrations = 50 and 100 μg/mL and = 3 mm at concentration = 150 μg/mL), (inhibition zone of $HL_8 = 3$ mm at

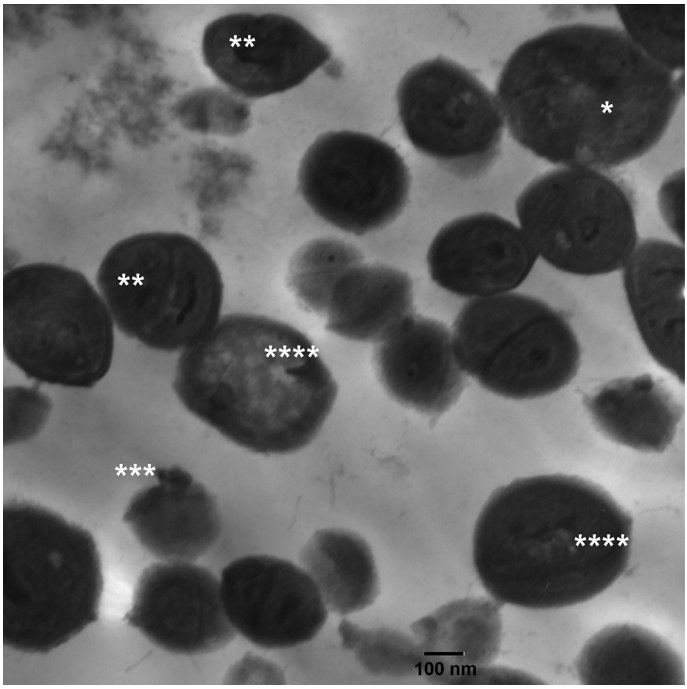

Fig. 17 Transmission electronic micrograph of *S. aureus* treated with ligand (HL_8) illustrating cocci cells, electron lucent or damaged boundary cell wall, numerous ribosomes (*single asterisks*), electron dense granules (*double asterisks*), granular cell contents appear to be exuding from the damaged membrane (*triple asterisks*), vacuoles of electron lucent regions are formed in the cytoplasm (*four asterisks*). (Specimen fixed in $_4F_1G$ solution and double-stained with uranyl acetate and lead citrate; original magnification ×7500)

concentrations = 100 and 150 μg/mL), (inhibition zone of HL_9 = 2 mm at concentrations = 50, 100 and 150 μg/mL) and (inhibition zone of HL_{10} = 3 mm at concentrations = 50 and 100 μg/mL and = 4 mm at concentration = 150 μg/mL). Addition to that *K. pneumoniae* was also weekly affected by $HL_{6–10}$ (inhibition zone of HL_6 = 1 mm and HL_9 = 2 mm at concentration = 150 μg/mL), (inhibition zone of HL_7 = 2 mm and = 1 mm at concentrations = 100 and 150 μg/mL, respectively) and (inhibition zone of HL_{10} = 1 mm at concentrations = 50, 100 and 150 μg/mL, respectively) as shown in Fig. 10. $HL_{6–10}$ ligands were found to have antibacterial activity against *E. coli* than against *K. pneumoniae*, and HL_{10} has high activity more than other ligands as shown in Figs. 11 and 12. HL_{10} is more active than penicillin against *E. coli* and *K. pneumoniae, w*hereas the HL_n and their derivatives have no effect against Gram-positive bacteria.

As shown in Table 7, the values of inhibition zones for ligands ($HL_{6–10}$) are related to the nature of the *p*-substituent as they increase according to the following order: *p*-(NO_2 > Cl > H > CH_3 > OCH_3) [25]. This can be attributed to the fact that the effective charge experienced by the d-electrons increased due to the electron-withdrawing *p*-substituent (HL_9 and HL_{10}) while it decreased by the

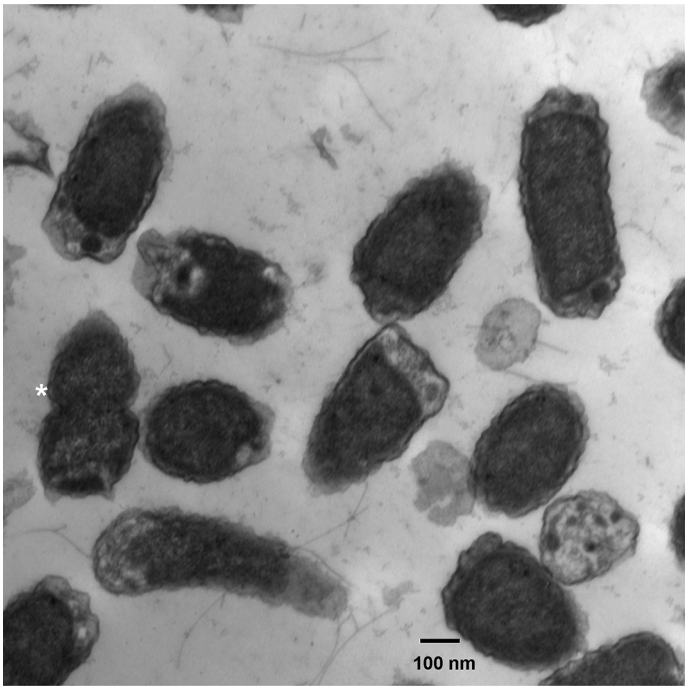

Fig. 18 Transmission electronic micrograph of normal *E. coli* showing rod shaped cells, normal smooth continuous cell wall and cell membrane, homogenous electron dense cytoplasm, normal electron lucent region between cell wall and cell membrane and normal cell division (*single asterisks*). (Specimen fixed in $_4F_1G$ solution and double stained with uranyl acetate and lead citrate; original magnification ×7500)

electron-donating character of (HL_6 and HL_7). This is in accordance with that expected from Hammett's substitution coefficients (σ^R) as shown in Fig. 13a, b. Correlating the values of inhibition zone (mm) with σ^R, it is clear that these values increase with increasing σ^R. It is important to note that the existence of a methyl and/or methoxy group enhances the electron density on the coordination sites and simultaneously decreases the values of inhibition zone.

The results in Table 7 reveal that the azo Schiff base ligands are moderately toxic against Gram-positive bacteria. Both ligands ($HL_{6–10}$) are more active against *E. coli* and *K. pneumoniae*.

Patel [33] found that 5-(4-N,N-diethylaminosulfonly phenylazo)-8-hydroxy quinoline and their metal chelates have moderate and high toxicity against some fungi including *Aspergillus niger* and *Penicillium expansum*. Our results of the antifungal activities of the azo Schiff base ligands ($HL_{6–10}$) are recorded in Table 8. The results of the examination of antifungal activity of $HL_{6–10}$ ligands revealed that the ligands have moderate toxicity against fungi.

The values of inhibition zone for ligands ($HL_{6–10}$) are shown in Table 8, $HL_{6–10}$ have antifungal activity against *A. alternata* (inhibition zone of $HL_6 = 5$ mm at concentration = 100 μg/mL), (inhibition zone of HL_7 and $HL_9 = 7$ mm at

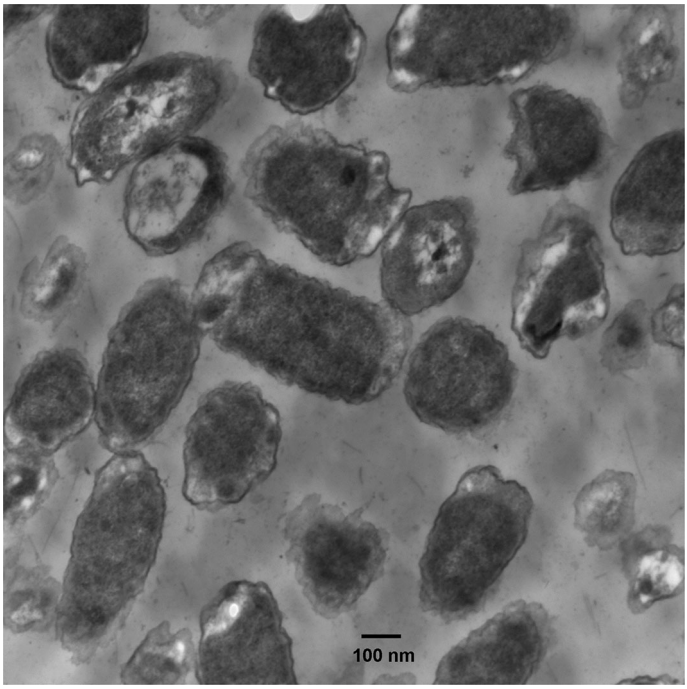

Fig. 19 Transmission electronic micrograph of *E. coli* treated with DMF showing rod shaped cells, normal smooth continuous cell wall and cell membrane, homogenous electron dense cytoplasm and normal electron lucent region between cell wall and cell membrane. (Specimen fixed in $_4F_1G$ solution and double-stained with uranyl acetate and lead citrate; original magnification ×7500)

concentration = 150 μg/mL) and (inhibition zone of HL_{10} = 7 mm at concentrations = 100 and 150 μg/mL) as shown in Table 8 and Fig. 14. In addition to that *P. italicum* was also affected by HL_n (inhibition zone of HL_6 = 4 and 2 mm at concentrations = 50 and 100 μg/mL, respectively), (inhibition zone of HL_7 = 5 mm at concentration = 50 μg/mL and = 1 mm at concentrations = 100 and 150 μg/mL), (inhibition zone of HL_8 = 5 and 3 mm at concentrations = 50 and 100 μg/mL, respectively), (inhibition zone of HL_9 = 1 mm at concentrations = 50 and 150 μg/mL) and (inhibition zone of HL_{10} = 3, 2 and 1 mm at concentrations = 50, 100 and 150 μg/mL, respectively). $HL_{6–10}$ have low antifungal activity against *F. oxysporum* (inhibition zone of HL_7 and HL_{10} = 1 mm at concentration = 100 μg/mL) and (inhibition zone of HL_8 and HL_9 = 3 mm at concentrations = 150 and 100 μg/mL, respectively).

The results of the TEM comparative study on the morphology and internal ultrastuctures; of normal and HL_8-treated *E. coli* and *S. aureus* provided strong evidence that HL_8 is stressful and toxic for the bacterial cells. In general, treatment of *E. coli* with HL_8 resulted in significant morphometric changes, whilst similar exposure of *S. aureus* produced no significant morphometric changes (Table 9). However, HL_8 prevents *S. aureus*' ability to adapt by reducing size, as shown in Fig. 15, and thickening the cell walls was seen with DMF treatment (Table 9). In

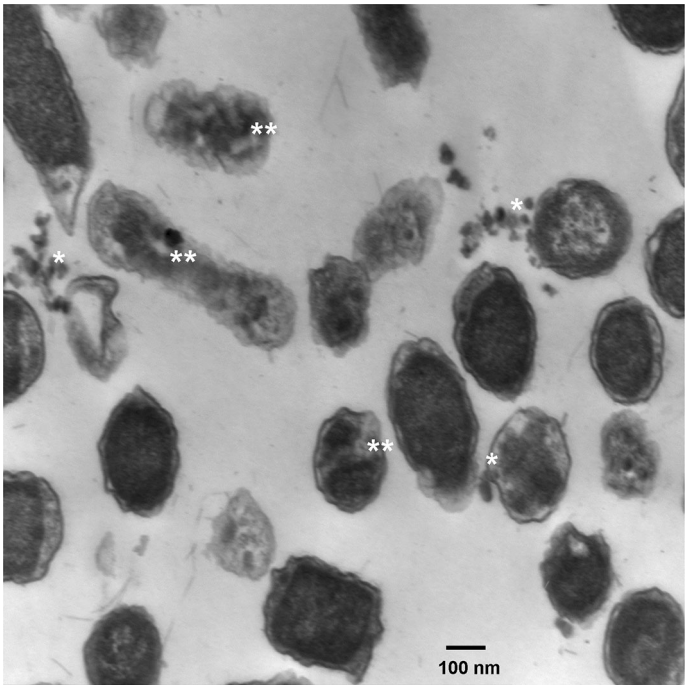

Fig. 20 Transmission electronic micrograph of *E. coli* treated with ligand (HL_8) showing malformed cells with rough irregular cell wall, granular cell contents appear to be exuding from the damaged membrane (*single asterisks*) and vacuoles of electron lucent regions are formed in the cytoplasm (*double asterisks*, *four asterisks*). (Specimen fixed in $_4F_1G$ solution and double-stained with uranyl acetate and lead citrate; original magnification ×7500)

the case of DMF treatment, *S. aureus* could resist the stressful conditions and keep its cell structure by thickening the cell walls and accelerating its cell division (Fig. 16). On the other hand, HL_8-treated *S. aureus* cell walls then appear electron lucent and damaged in some cells (Fig. 17). Internal cell components of *S. aureus* in the case of DMF are kept stable although some electron dense granules appear in the cytoplasm (Fig. 16), whereas HL_8 treatment leads to *S. aureus* cell damaged at all in different stages. These stages include electron dense granules and electron lucent vacuoles formation in the cytoplasm, weakening and damaging of the boundary cell wall and finally granular cell contents exudes from the damaged membrane. The *E. coli,* DMF treatment did not result in any significant cytomorphological changes (Figs. 18, 19), whereas HL_8 treatment was found to significantly reduce the width of the *E. coli* cells (Table 9) resulting in malformed cells (Fig. 20). Furthermore, the main effect of HL_8 begins in the cytoplasm by vacuolation then damages the cell wall (Fig. 20) without affecting the distance between the cell wall and the cell membrane (Table 9). TEM examination of HL_8-treated *E. coli* and *S. aureus* confirmed that HL_8 has a bactericidal effect against both bacteria, as granular cell contents appear to exude from the damaged cell membrane (Figs. 17, 20) [34–37].

Conclusion

Azo ligands (HL_n) (where $n = 1–5$), azo Schiff base ligands (HL_n) (where $n = 6–10$) were synthesized and characterized by elemental analysis, IR, ^{1}H NMR, X-ray diffraction analysis, mass spectra and thermal studies. The azo quinoline ligands [5-(4′-derivatives phenyldiazo)-8-hydroxy-7-quinolinecarboxaldehyde[$HL_{1–5}$ are a mixture of amorphous and polycrystalline structures while azo Schiff base ligands 4-{[5-(4-substituted-phenylazo)-8-hydroxy-quinolin-7-ylmethylene]-amino}-1,5-dimethyl-2-phenyl-1,2-dihydro-pyrazol-3-one derivatives $HL_{6–10}$ are completely amorphous. The molecular ion peaks of HL_2 and (HL_6, HL_8 and HL_9) are in good agreement with their suggested empirical formulae as indicated from elemental analyses. The variation of azo and azomethine groups strongly affected the decomposition behavior and the values of thermal activation energy E_d of decomposition. The antimicrobial activity was tested against *B. cereus*, *S. aureus*, *E. coli*, *K. pneumoniae*, *A. niger*, *F. oxysporum*, *A. alternata* and *P. italicum*. The antimicrobial tests proved that none of the used azo compounds have any antimicrobial activity, while both tested azo Schiff base compounds have antibacterial activity on *E. coli* and *K. pneumoniae* and antifungal activity on *A. alternata*, *A. niger* and *P. italicum*. Ultrastructure study of affected *E. coli* and *S. aureus* confirmed that HL_8 has antibacterial activity.

Acknowledgments The authors would like to thank Prof. Dr. Nabila El-Sayed Abdel Meguid Prof. Emeritus of Cytology and Cytochemistry, Zoology Department, Faculty of Science, Alexandria University, Egypt and Miss N.F. Omar, Botany Department, Faculty of Science, Damietta University, Egypt for their help during testing antimicrobial activities and ultrastructure study.

Compliance with ethical standards

Ethical statement On behalf of the authors of our paper entitled "Dielectrical properties and conduction mechanism of quinoline Schiff base and its complexes", we certify that this paper is abstracted from our own work. This work is carried out in our laboratory and the obtained results have not been published in any journals. We have not received any grant from any agencies or company. We state that we do not have any conflict of interest with anyone.

References

1. H. Zollinger, *Color Chemistry* (VCH, Weinheim, 1991)
2. K.T. Chung, C.E. Cerniglia, Mutat. Res. **277**, 201–220 (1992)
3. K.T. Chung, S.E.J. Stevens, Environ. Toxicol. Chem. **12**, 2121–2132 (1993)
4. P.K. Wong, P.Y. Yuen, Water Res. **30**, 1736–1744 (1996)
5. D.N. Dhar, C.L. Taploo, J. Sci. Ind. Res. **41**, 501–506 (1982)
6. P. Przybylski, A. Huczynski, K. Pyta, B. Brzezinski, F. Bartl, Curr. Org. Chem. **13**, 124–148 (2009)
7. C.M. da Silva, D.L. da Silva, L.V. Modolo, R.B. Alves, M.A. de Resende, C.V.B. Martins, Â. de Fátima, J. Adv. Res. **2**, 1–8 (2011)
8. K.I. Bhat, R.V. Kumar, B. Kalluraya, Asian J. Chem. **16**, 96–102 (2004)
9. G.K. Rao, R. Kaur, P.N.S. Pai, Der Pharm. Chem. **3**, 323–329 (2011)
10. A.A. Jarrahpour, M. Motamedifar, K. Pakshir, N. Hadi, M. Zarei, Molecules **9**, 815–824 (2004)
11. M. Zarei, A. Jarrahpour, Iran. J. Sci. Technol. **A3**, 235–242 (2011)
12. S. Eswaran, A.V. Adhikari, N.S. Shetty, Eur. J. Med. Chem. **44**, 4637–4647 (2009)
13. C. Caris, P. Baret, J.L. Pierre, G. Serratrice, Tetrahedron **52**, 4659–4672 (1996)

14. K.H. Lam, R. Gambari, K.K.H. Lee, Y.X. Chen, S.H.L. Kok, R.S.M. Wong, F.Y. Lau, C.H. Cheng, W.Y. Wong, Z.X. Bian, A.S.C. Chan, J.C.O. Tang, C.H. Chui, Bioorg. Med. Chem. Lett. **24**, 367–370 (2014)
15. M. El-Behery, H. El-Twigry, Spectrochim. Acta A **66**, 28–36 (2007)
16. M.I. Abou-Dobara, M.A. Diab, A.Z. El-Sonbati, A.M. Barakat, Arab. J. Chem. (2013). doi:10.1016/j.arabjc.2013.03.018
17. A.Z. El-Sonbati, A.A. El-bindary, A.F. Shoair, R.M. Younes, Chem. Pharm. Bull. **49**, 1308–1313 (2001)
18. A.Z. El-Sonbati, A.A. El-bindary, Polish J. Chem. **74**, 621–630 (2000)
19. N.A. El-Ghamaz, M.A. Diab, A.A. El-Bindary, A.Z. El-Sonbati, S.G. Nozha, Spectrochim. Acta A **143**, 200–212 (2015)
20. M.M. El-Nahass, H.S. Soliman, N. El-Kadry, A.Y. Morsy, S. Yaghmour, J. Mater. Sci. Lett. **7**, 1050–1053 (1988)
21. N.A. El-Ghamaz, M.A. Diab, A.A. El-Bindary, A.Z. El-Sonbati, S.G. Nozha, Solid State Sci. **30**, 44–54 (2014)
22. M.A. Diab, A.Z. El-Sonbati, A.A. El-Bindary, A.M. Barakat, Spectrochim. Acta A **116**, 428–439 (2013)
23. M.A. Diab, A.A. El-Bindary, A.Z. El-Sonbait, O.L. Salem, J. Mol. Struct. **1018**, 176–184 (2012)
24. N.A. El-Ghamaz, M.A. Diab, A.Z. El-Sonbati, O.L. Salem, Spectrochim. Acta A **83**, 61–66 (2011)
25. M.I. Abou-Dobara, A.Z. El-Sonbati, ShM Morgan, World J. Microbiol. Biotech. **29**, 119–126 (2013)
26. A.Z. El-Sonbati, A.A.M. Belal, M.S. El-Gharib, ShM Morgan, Spectrochim. Acta A **95**, 627–636 (2012)
27. A.W. Coats, J.P. Redfern, Nature **20**, 68–79 (1964)
28. H.W. Horowitz, G. Metzger, Anal. Chem. **35**, 1464–1468 (1963)
29. A.Z. El-Sonbati, M.A. Diab, A.A. El-Bindary, A.M. Eldesoky, ShM Morgan, Spectrochim. Acta A **135**, 774–791 (2015)
30. M.M. Ghoneim, A.Z. El-Sonbati, A.A. El-Bindary, M.A. Diab, L.S. Serag, Spectrochim. Acta A **140**, 111–131 (2015)
31. E.W. Koneman, Koneman's Color Atlas and Textbook of Diagnostic Microbiology, 2006
32. B. Forbes, Bailey and Scott's Diagnostic Microbiology - Elsevier eBook on VitalSource, 12th Edn, 2002
33. A.U. Patel, E-J. Chem. **6**, 1247–1252 (2009)
34. G. Neumann, Y. Veeranagouda, T.B. Karegoudar, O. Sahin, I. Mausezahl, N. Kabelitz, U. Kappelmeyer, H.J. Heipieper, Extremophiles **9**, 163–168 (2005)
35. G.W. O'Hara, A.R. Glenn, Arch. Microbiol. **161**, 286–292 (1994)
36. M. Ritz, J.L. Tholozan, M. Federighi, M.F. Pilet, Appl. Environ. Microbiol. **67**, 2240–2247 (2001)
37. M.I. Abou-Dobara, A.Z. El-Sonbati, M.A. Diab, A.A. El-Bindary, ShM Morgan, J. Microbial. Biochem. Technol. (2014). doi:10.4172/1948-5948.S3-006